Partial Liquid Alloy Microdroplet Sedimentation Induced a Gradient Porous Structured Elastomer with a Tunable Property for an Anisotropic Robotic Bulk

Shuo Zhang,*,† Zisheng Zong,† Chuan Fei Guo, Han Ding, and Zhigang Wu*

Cite This: *ACS Appl. Mater. Interfaces* 2022, 14, 50079−50089

Read Online

ACCESS | Metrics & More | Article Recommendations | Supporting Information

ABSTRACT: With the confrontation of ever increasing complicated working objects and unstructured environments, it is necessary for soft robots to be equipped with diverse intelligent mechanical structures, for example, anisotropically motorial bulk and timely proprio/exteroceptive sensing with programmable morphologies. Owing to abundant pores inside, porous media are promising to host various intelligent functions as interfaces/structures of robots yet challenging because of a limited anisotropic response inherited from a random hierarchical pore distribution. Here, an electron competition between Ga, N, and Pt is found and used to tune the polymerization of a gradient liquid alloy and NH_4HCO_3-suspended silicone precursor mixture and, thus, decompose gas movements in gradient pore formation under high-temperature heating (120 °C). By such a competition−collaboration effect, we present here an interconnected gradient porous structure (GPS) that can serve as an anisotropically robotic motorial bulk. Moreover, the mechanical stiffness and piezoresistive/capacitive property of GPS can be further tuned and reconfigured via so-called self-sucked coating, following solvent erasing. Such new structures provide a dynamic tactile recognition with an ultrabroad sensing range (from 135 Pa to 2.3 MPa) and a reconfigurable biomimetic elephant trunk with monolithic proprioceptive sensing-integrated bulks.

KEYWORDS: liquid alloy, electron competition, gradient pores, tunable stiffness and sensitivity, monolithic sensing-integrated structure
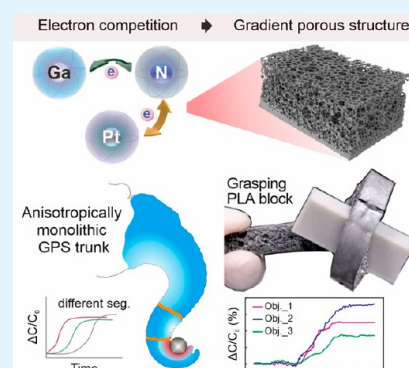
INTRODUCTION

A controllable compliant bulk with programmable morphology, tunable stiffness, integratable sensing, and anisotropic response when being continuously deformed is one of the fundamental keys to enhance interaction capabilities of soft robots along their movements.[1−4] While in nature, monolithically proprioceptive sensing-integrated structures widely exist for intelligent interaction with the external environment, for example, an elephant trunk, octopus tentacle, and human muscle, and exhibit premium performance in many complicated interaction scenarios. To achieve such intelligent structures, subtle and novel designs of heterogeneous, anisotropic, hierarchical, and multifunctional materials/structures have been sedulously pursued.[5−7] With inspiration from natural living organisms and systems, porous structures are not only extensively exploited for energy conversion and storage,[8] reaction catalysis,[9] and surface energy tuning[10,11] but also of great potential for developing bionic and biomimetic interfaces/structures as a result of the distinctive properties of a hierarchically large accessible space and high surface area.[12−18] Elaborate fabrication strategies, templating methods,[19] physical and chemical techniques, and (multiphase or soluble) sacrificial media separation[20] have been extensively investigated.[21] Although these strategies have established dual or multiple porosity with a time-consuming process, the size of

the pore still ranges from nanoscale to a few micrometers, which is inadequate for micrometer- or even millimeter-scale application in soft robots. Moreover, current porous structures are mostly with a random hierarchical pore distribution that are overall homogeneous. Such a homogeneous porosity severely restricts the anisotropic interaction when the porous structure is acting as a deformable bulk or interface, e.g., human−machine interface, artificial-graded structures, and compliant mechanism in soft robots.[16,22]

Alternatively, additive manufacturing, e.g., three-dimensional (3D) printing or layer-by-layer depositing/stacking, is possible to configure gradient macroscopic pores, and nevertheless, it heavily depended upon specific developed materials or dedicated equipment.[23,24] Some researchers used cost-effective approaches via chemical reaction with phase transition, e.g., ammonium hydrogen carbonate (NH_4HCO_3) as gas foaming and other porogens.[25−27] It may not be suitable for platinum
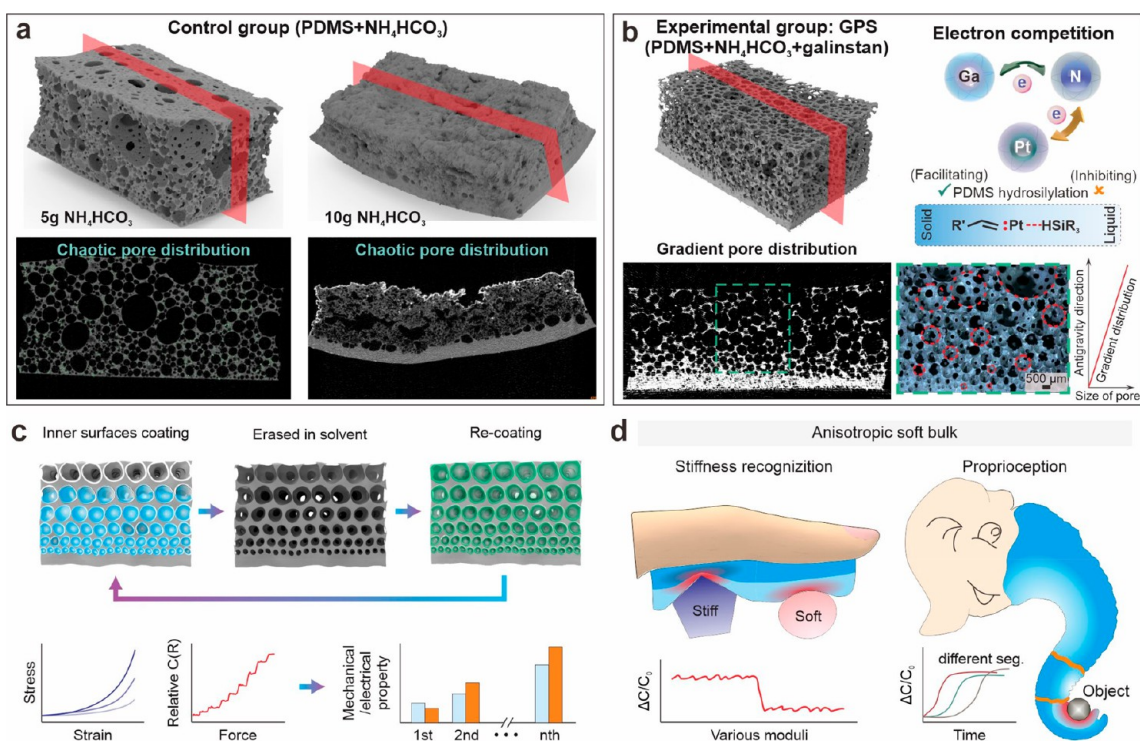
Figure 1. Overview of the gradient porous structure. (a) Micro-computed tomography (μCT)-reconfigured 3D constructions and vertical sections of the control group. (b) μCT-reconfigured 3D construction and vertical section of the experimental group. The upper right is a conceptual illustration of electron competition between gallium, platinum, and nitrogen. The enlarged view is the optical image. (c) Schematic of enabling and reconfiguring functionality via self-sucked coating. (d) Schematic of an anisotropic soft robotic bulk for recognizing and grasping objects. The deep color represents small porosity, while the light color represents large porosity.

(Pt)-catalyzed silicone rubber that is widely used in the bulk of soft robots, e.g., polydimethylsiloxane (PDMS), because introduced amino would hinder the polymerization of PDMS.[28] Thus, there is still a lack of effective mechanics to tune and modify PDMS bulk into a programmable porous structure. Besides, it is still challenging to achieve a micrometer-scale porous structure with tunable gradient porous morphology and, hence, adjustable mechanical and electrical properties in a controllable way.

In this work, as briefly shown in Movie S1 of the Supporting Information, in comparison to chaotic pore-distributed PDMS, which is obtained by mixing with NH_4HCO_3, we present gradient porous-structured PDMS obtained by mixing with a liquid alloy (galinstan) and NH_4HCO_3 (Figure 1a). By investigation of an electron competition mechanism between elements Ga, N, and Pt in a gradient gallium-based liquid alloy (LA) and NH_4HCO_3 suspended multiphase mixture of gallium-based LA, NH_4HCO_3, and PDMS precursor, the pore formation can be tuned together with the silicone hydrosilylation reaction under relatively high temperature (120 °C) heating (Figure 1b). Such a competition−collaboration mechanism contributes to tuning the catalysis activity of Pt, which results in a gradient porous structure (GPS) formation with an interconnected anisotropic pore distribution and size ranging from 80 μm to 3.2 mm approximately (Figure 1b and Figure S1 of the Supporting Information). Considerably, a self-sucked coating followed with a solvent-erasing process is further proposed for endowing and reconfiguring functionalities (mechanical stiffness and electrical property) (Figure 1c). Such a coated GPS provides a distinguished sensing of the porous tactile interface and a proprioceptive sensing-integrated soft biomimetic elephant trunk (Figure 1d). The presented

GPSs offer soft robots new anisotropic high-performance bulk/ structures with large accessible space for monolithic integration of more functions to strive for higher performance or intelligence. This work not only opens a promising window of investigating the catalysis of Ga and enriches the fields of characteristics of liquid metal, but a competition−collaboration mechanism also encourages the development of tunable, programmable, and anisotropic material/structure fabrication.

◼ MATERIALS AND METHODS

Fabrication Process. Liquid alloy (galinstan, Geratherm Medical AG, Geschwenda, Germany) bulk was spread into a large thin film by a mixing defoamer (ARE-310, Thinky, Japan, 800 rpm for 1 min, 1200 rpm for 30 s, 1600 rpm for 1 min, and 1800 rpm for 30 s) and then mixed with a silicone base of PDMS (Sylgard 184, Dow Corning Corporation) at the ratio of 1:20 by the defoamer with the same process to form a suspension distributed with μ-LA particles. Ammonium hydrogen carbonate (A18566, 98%, Alfa Aesar, Shanghai, China) was finely ground into μ powder by ball milling (MSK-SFM-3, HF-Kejing, China) and then mixed with the suspension mixture at the ratio of 10:21 using the defoamer. Next, the curing agent was added and mixed via the defoamer under the same process. The composite mixture was placed at 20 °C for ~12 h, following heated in an oven (UF55 Plus, Memmert, Germany) at 120 °C for 1.5−3 h.

Characterizations. A stereoscopic microscope (Stemi 508, Carl Zeiss, Germany) was used to observed the profile of GPS. The pore distribution was measured under a digital microscope (PQV-100, SHPQYQ, China). The GPS was dyed with nano-Fe_3O_4 powder (I811859, 99.5%, 20 nm, Maclkin, U.S.A.) for cross-sectional imaging. The contrast, lightness, and area of images were processed with the ImageJ program, and then edges were fitted using AutoCAD (Autodesk Inventor Professional 2022). Finally, MATLAB (R2020b, MathWorks, Natick, MA, U.S.A.) was used to extract the distribution information (radius and coordinate value). Micro-computed tomog-
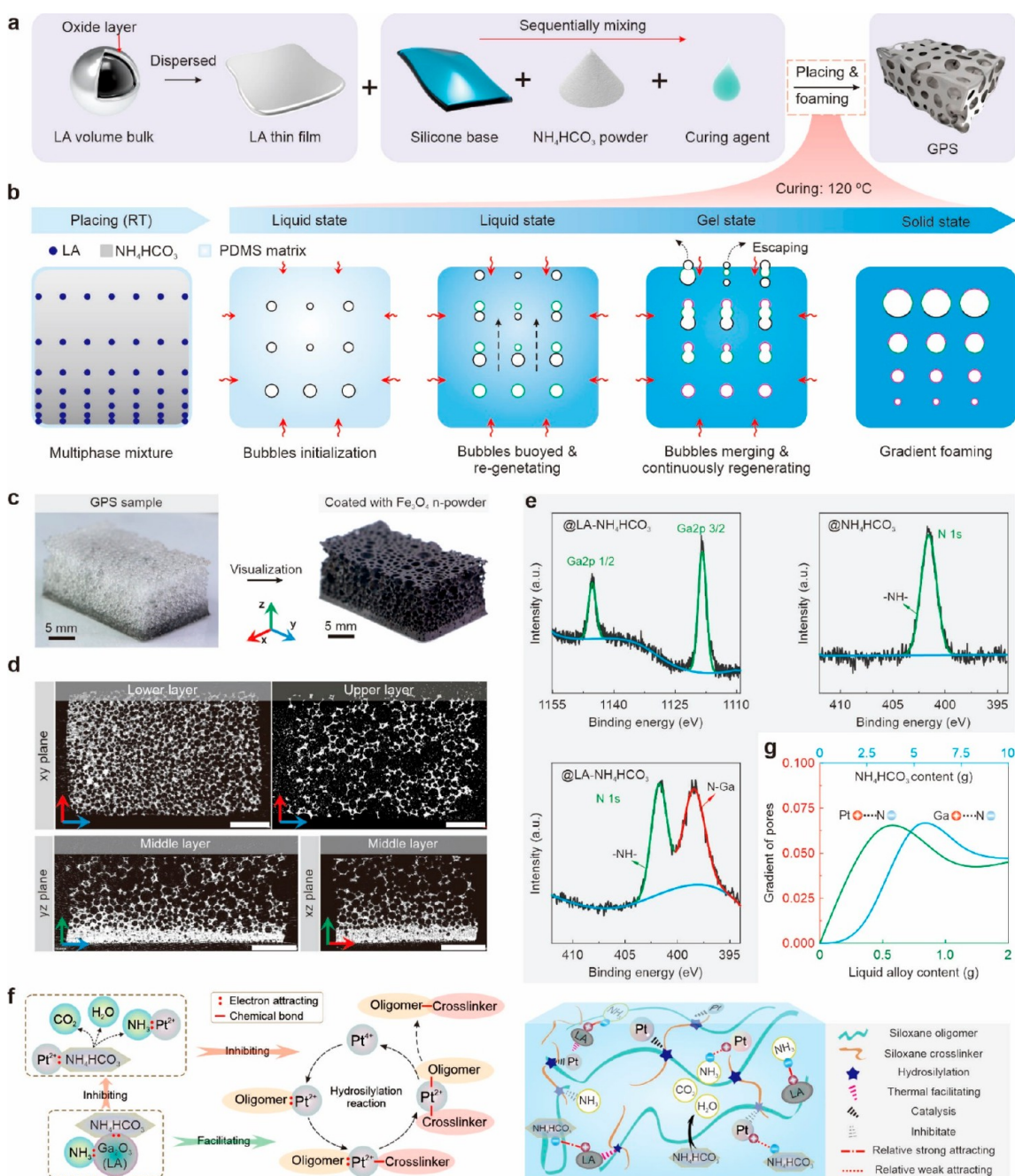
Figure 2. Fabrication process and foaming mechanism. (a) Schematic of the fabrication process. (b) Schematic of the multiphase mixture after being placed for 12 h at room temperature, and gradient pore foaming process under 120 °C for 3 h. (c) Optical images of a pristine GPS (upper) and nano-Fe_3O_4 particle-dyed GPS (lower). (d) 3D μCT-reconfigured pore distribution. Scale bars = 5 mm. (e) XPS spectra (Ga 2p and N 1s) of the mixture of LA (galinstan) and NH_4HCO_3 and the control group of NH_4HCO_3. (f) Schematic of detailed reactions between different components (left panel) and their contribution to the competitive mechanism in the PDMS matrix (right panel). (g) Relationship between the gradient of porosity and the content of LA and NH_4HCO_3.

raphy (SkyScan 1176, Bruker, Germany) was used to reconfigure the detailed pore distribution of GPS. Field scanning electron microscopy (FSEM, Nova Nano SEM 450, FEI, Netherlands) was used to obtain energy-dispersive X-ray (EDX) detector data (elements and distributions) of the GPS coated with LA and poly(vinyl alcohol) (PVA). X-ray photoelectron spectroscopy (XPS, AXIS Supra$^+$, Kratos, Japan) was used to identify the reaction between LA and NH_4HCO_3. The compression test was conducted with a universal testing system (5944, Instron, Boston, MA, U.S.A.). The electrical capacitance/resistance and dielectric permittivity of sensors were measured with a precision LCR meter (E4980AL, Keysight Technologies, Santa Rosa, CA, U.S.A.) connected with a dielectric fixture (16451B, Keysight

Technologies, Santa Rosa, CA, U.S.A.). A force gauge (HP-5, Yueqing Handpi Instruments, China) and a dynamic testing instrument (E1000, Instron, Boston, MA, U.S.A.) were used to apply a normal force.

Self-Sucked Coating and Reconfiguring Function. PVA (0588, Aladdin, Shanghai, China) aqueous solution (10−30 wt %) was prepared using a magnetic mixer (HS 7, IKA, Germany) for 30 min at 120 °C. A total of 3, 6, and 9 g of PVA powder and 0.6, 2.4, and 2.4 g of tannin acid [molecular weight (Mw) of 1701.23, BKMAN, Changde, China] were added to 27, 24, and 21 g of deionized water. The GPS was placed in a Petri dish filled with PVA solution. With continuous pressing of the GPS, the PVA solutions

were filled into the bulk thoroughly and then heated for 1 h at 105 °C to evaporate water. The LA, dimethyl silicone oil (Alibaba, China), and writing ink were coated with the same process. The dynamic viscosity of the coating solution was measured with a viscometer (DV2T, Brookfield, Middleboro, MA, U.S.A.). The surface tension was measured with a surface tension meter (BZY-2, Shanghai Hengping Instruments, China). For coating erasure, poly(glycerol sebacate) (PGS) (with PVA) was placed in water (80 °C) on a magnetic stirrer for 10 min to dissolve PVA. The coated LA was erased with a sodium hydroxide aqueous solution (NaOH, 1.25 M, 10019718, SCR, Shanghai, China).

Demonstrations. For capacitive sensors, conductive fabric electrodes (from Alibaba, China) were clamped between two polyethylene terephthalate (PET) substrates (YH-2910, Yuanhao, Shanghai, China). Subsequently, the electrodes were glued onto the porous structure with adhesive rubber (Sil-Poxy, Smooth-On, Macungie, PA, U.S.A.) and heated at 90 °C in the oven. For resistive sensors, copper or conductive fabric electrodes were directly attached to the two ending surfaces of the GPS using silver paste (3703, SINWE, Shenzhen, China), and the PET sheets were glued to the copper electrodes for protection. The prosthetic hand and epoxy balls were from a commercial 3D printing service (WeNext Technology Co., Ltd., Shenzhen, China). The photographs of sensing various stiffness objects were taken with a camera (Canon EOS 70D, Tokyo, Japan). The impact test was conducted from a height of 30 cm and recorded using an ultrahigh-speed camera (Phantom V1212, Vision Research, Inc., Wayne, NJ, U.S.A.). The cocklebur, acrylic tubes, and glass balls were purchased from Alibaba, China. To fabricate multimodel sensors, the GPS was cut into the predesigned shapes and then coated with LA and poly(vinyl alcohol)−tannin (PVA−TA)/H_2O (10 wt %). The porous structure was heated in the oven for 1 h at 105 °C to evaporate water. Conductive fabric electrodes were attached to the two ends of the GPS. The anisotropic GPS trunk was fabricated as schematically illustrated in panels a and e of Figure 6. The GPS, PET, and conductive fabric were adhered by an adhesive rubber (Sil-Poxy). The soft and sticky PDMS-based composite (S3PDMS) was made by following the process in ref 28. The deformation was recorded with a digital camera (Canon EOS R5, Tokyo, Japan). The capacitance was measured by the LCR meter. The polylactic acid (PLA) block was obtained by a 3D printer (E3, HORI, Beijing, China).

RESULTS AND DISCUSSION

Gradient Foaming and Mechanism Investigation. To learn the gradient foaming mechanism, the fabrication process is illustrated in Figure 2a. Because Ga is an active metal, LA tends to form a thin layer of oxides (mainly Ga_2O_3) on its surface in ambient air,[29−31] while the miniaturization of LA in microparticles (Figure S2a of the Supporting Information) increases the total area of the oxide layer. Simultaneously, it also helps to improve its uniformity in the mixture with silicone base. Meanwhile, NH_4HCO_3 flakes were ground into 1−10 μm (Figure S2b of the Supporting Information) to improve the dispersibility in the mixture. After room temperature for 12 h, LA and NH_4HCO_3 powders/particles were experiencing sedimentation, forming a gradient distribution of them in the multiphase mixture. In particular, because the size and density of LA are much larger than those of NH_4HCO_3, an obvious partial sedimentation of LA results with a slight partial sedimentation of NH_4HCO_3 during the 12 h rest (Figure 2b and panels a and b of Figure S3 of the Supporting Information). Such a heterogeneous sedimentation further induces a non-uniformity of thermal conductivity and bubble initialization during a relatively high-temperature PDMS polymerization (120 °C, during which NH_4HCO_3 can be decomposed into gases thoroughly).

At the beginning, as a result of thermal decomposition of NH_4HCO_3, there are tiny bubbles sequentially initializing (black circles) from the periphery to center along the direction of thermal conduction. As observed, with continuous heating at 120 °C, the multiphase mixture still exhibits a liquid state (panels c and d of Figure S3 of the Supporting Information) and new bubbles (green circles) maintain initialization as a result of continuous thermal decomposition and float up as a result of buoyance force. In liquid, the earlier initialized isolated bubbles contact each other and merge into bigger bubbles along the antigravity direction, while at the same time, new bubbles continue initializing near the old positions where earlier isolated bubbles initialized until the mixture became a gel state. An obvious gradient distribution of LA causes different extents of electron competition along the gravity direction, as discussed later, and, hence, different moving and merging behaviors of bubbles in that direction. Consequently, it finally results in an incremental gradient bubble size distribution along the antigravity direction. Once the mixture was fully cured into a solid state, interconnected gradient porosity was obtained (Figure 2c). Through μCT, reconstructed images clearly reflect a gradient pore distribution along the antigravity direction yet an isotropic distribution in the direction perpendicular to gravity (Figure 2d and Figure S4 of the Supporting Information). Notably, during the foaming process, NH_4HCO_3 powders nearly fill the PDMS matrix entirely, which provides more opportunities for widespread bubbles to freely move and contact, thus leading to an interconnected hollow construction.

During such a foaming process, a few competitive reactions coexist in the system and influence each other during the GPS formation. For NH_4HCO_3, (i) it can be thermally decomposed into carbon dioxide (CO_2), water (H_2O), and ammonia (NH_3), which promotes foaming. (ii) According to previous studies, PDMS employed here was polymerized with hydrosilylation catalyzed by a platinum (Pt) complex (Figure S5 of the Supporting Information) that is coordinatively unsaturated and, hence, forms strong complexes with strong electronegative chemical groups, e.g., amino in NH_4HCO_3.[28,32] As a result of such an electronegative effect, it can inhibit the PDMS polymerization process and elongate the curing time, even under a high temperature (here, 120 °C) (Figure S3c of the Supporting Information), and, thus, guarantee a liquid state of the mixture with a sufficient processing time window for initializing, floating, and merging/escaping of bubbles. For LA, (i) as a result of its excellent thermal conductivity, it would enhance the thermal conductivity of the mixture and accelerate the curing process in the case of all bubbles escaping. (ii) Because an alloy includes active metals, e.g., Ga, LA can offer abundant electrons to electronegative groups, such as amino, and, hence, reduce their inhibition effects on PDMS polymerization. Such an electron-donating effect can be clearly observed in XPS spectra (Figure 2e). In comparison to a control group (only with NH_4HCO_3), the obtained XPS spectra of the mixture with both LA and NH_4HCO_3 show a new absorption peak (fitted red curve), which refers to an electron attraction between −NH− and Ga_2O_3. In addition, it has also been reported that amine groups are able to chelate with metal cations, e.g., Ga^{3+}, based on electrostatic interactions.[33−35] Further, according to the metal active order, Ga is more active than Pt when interacting with electronegative elements. Therefore, the introduced LA can attract the N element and, hence, weaken the inhabitation
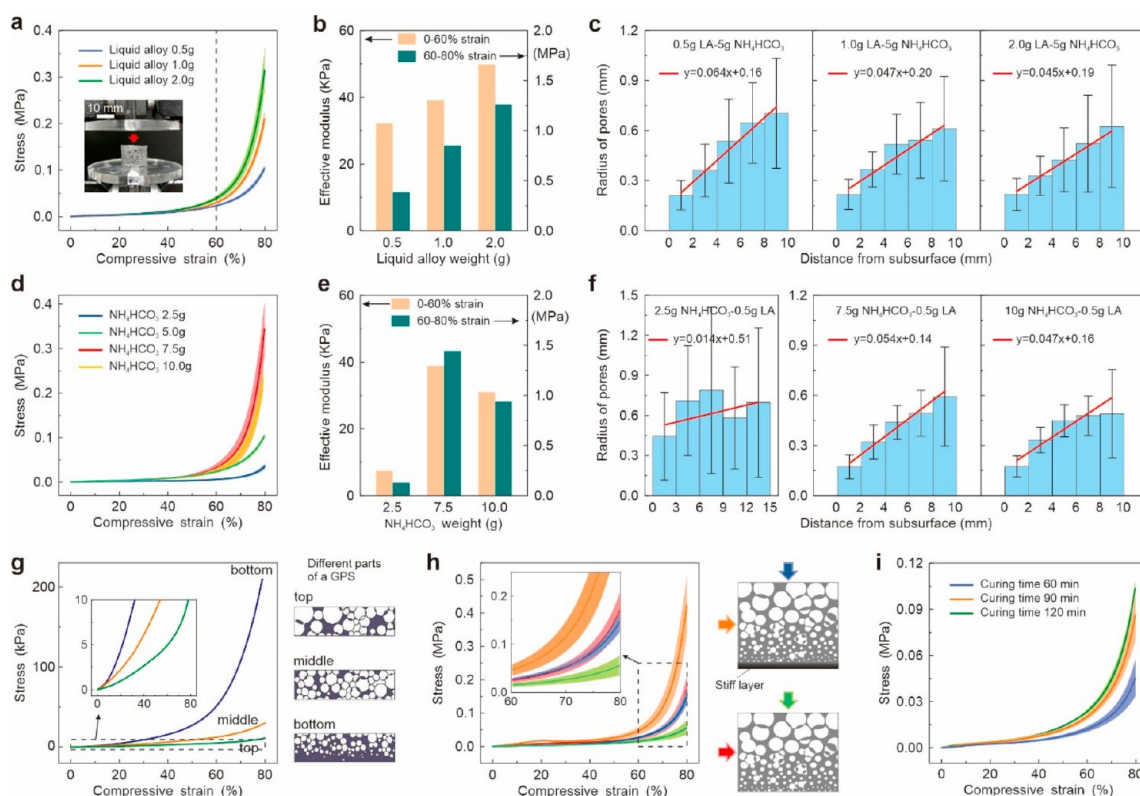
Figure 3. Mechanical characterizations. (a) Stress−strain curves of GPS obtained with different contents of LA with 5.0 g of NH_4HCO_3. The inset indicates the measurement setup. (b) Piecewise effective compressive moduli at 0−60 and 60−80% compressive strain derived from panel a. (c) Corresponding statistic of the pore distribution versus the distance from the subsurface. (d) Stress−strain curves of GPS obtained with different contents of NH_4HCO_3 with 1.0 g of LA. (e) Piecewise effective compressive moduli derived from panel d. (f) Corresponding statistic of the pore distribution versus the distance from the subsurface. (g) Compressive stress−strain curves and schematic of different parts of a GPS. (h) Compressive stress−strain curves obtained from applying different press directions (illustrated by colorful arrows). (i) Stress−strain curves according to different curing times.

effect of NH_4HCO_3/NH_3 on the Pt catalyst complex, ultimately facilitating the curing process.

In brief, in such a multiparty coexisting system, for PDMS curing, N strongly attracts electrons and, hence, inhibits PDMS polymerization to keep it as a liquid state in a relatively longer time window, which allows the bubble size to grow along the antigravity direction and, hence, facilitates gradient pore formation. In contrast, Ga can neutralize such an inhibition and, hence, accelerate PDMS polymerization toward a solid state (Figure 2f), which subsequently helps to "freeze" bubbles inside the finally cured PDMS matrix. More importantly, as 12 h sedimentation induces an obvious LA gradient distribution along the gravity direction, and LA facilitates a gradient PDMS polymerization along the antigravity direction. Therefore, in the presence of a LA particle gradient, the two competitive electron donor reception behaviors among the LA, NH_4HCO_3, and Pt catalyst in the silicone precursor mixture collaboratively form a gradient porous structure in PDMS. In contrast, as a reference, in a series of control experiments with $NaHCO_3$ that lack the N element, a poor foaming and gradient porosity is found (Figures S6 and S7 of the Supporting Information).

Furthermore, the gradient of pores can be tuned by adjusting the content of LA and NH_4HCO_3 (Figure 2g). With an increasing NH_4HCO_3 content (0−5 g), the thermal decomposition is facilitated, resulting in an increasing pore gradient. In contrast, with continuously more NH_4HCO_3 (>5 g), it inhibits the Pt catalyst, and hence, the gradient decreases because an overly long liquid state also results in bubbles

escaping. With regard to LA, when its content was less than 0.5 g, the gradient of pores increases as a result of neutralizing −NH−. However, more LA content (1 and 2 g) brought a decreased pore gradient as a result of significant enhancement of thermal conductivity. Hence, a trade-off between various introduced contents is necessary for specific situations or purposes. Such a tuning effect with different combinations of LA and NH_4HCO_3 can be observed as well in the cross-sectional images of GPSs (Figure S8 of the Supporting Information).

Gradient Structure Enabled Mechanical Behaviors. As a benefit from its gradient construction, GPS exhibits anisotropic mechanical properties under compression (Figure 3a), following the corresponding effective compressive moduli in Figure 3b. Generally, the stress increases with more LA, suggesting an incremental stiffness. Specifically, at a strain of 0−60%, the effective moduli were less than 50 kPa, while with continuous compression to 60−80%, the effective moduli significantly increase over 1 MPa because of the contribution from the small-sized pores at the lower layer. For detailed structure configuration, a statistic pore distribution is in Figure 3c and Figure S9 of the Supporting Information, together with the images in Figure S8 of the Supporting Information. The GPS (0.5 g of LA) shows a steeper pore distribution gradient than that with 1.0 and 2.0 g of LA, which contributes to large-size pores at the upper layer and, thus, a small effective modulus. With more LA, the thermal conduction of the mixture is higher, and hence, it results in a shorter curing time,
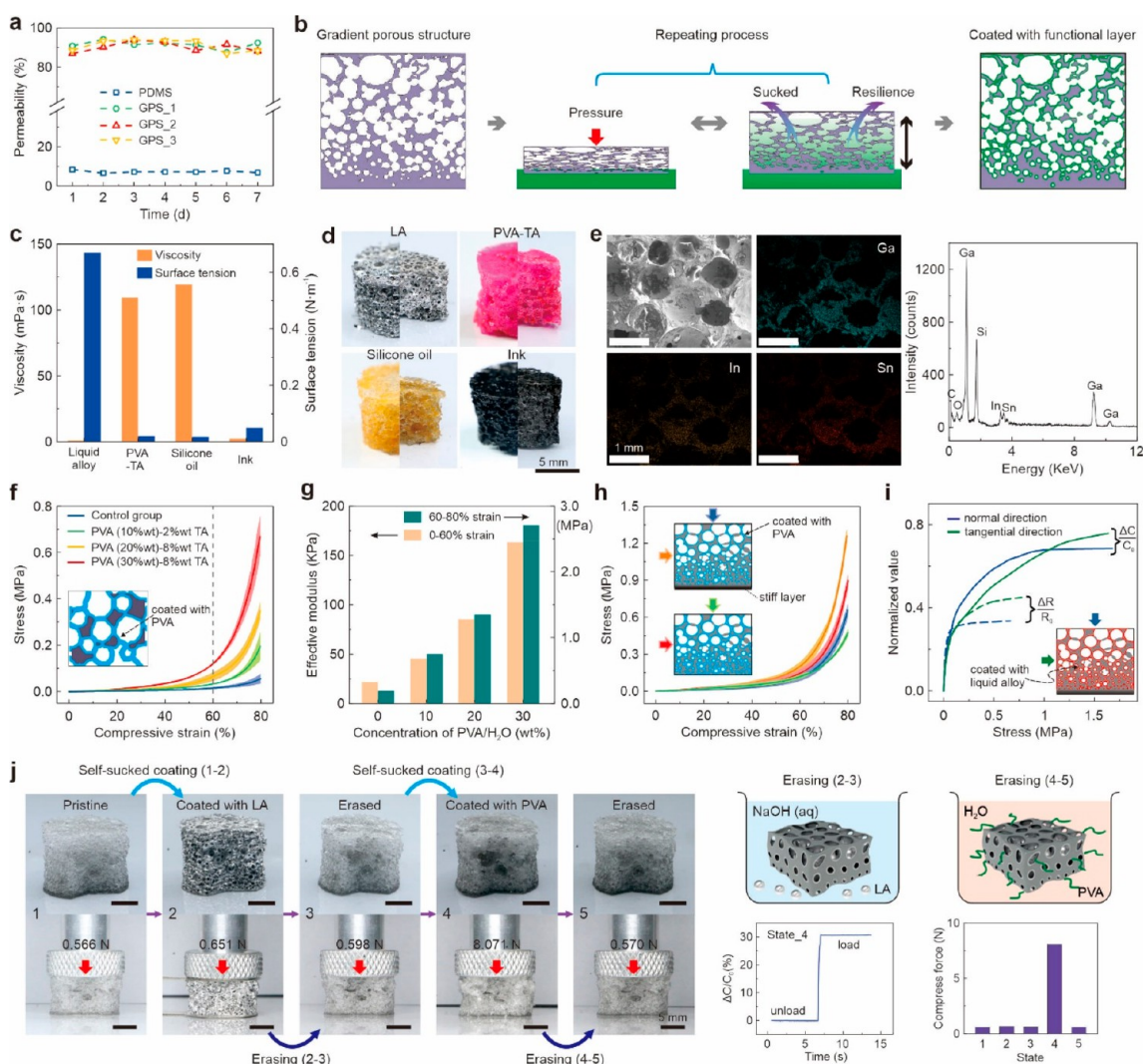
Figure 4. Enabling functions via self-sucked coating. (a) Air permeability conducted for 7 days. (b) Schematic illustration of the self-sucked coating process. (c) Viscosity and surface tension of various solutions. (d) Overall view (left) and sectional view (right) of samples coated with LA, PVA−TA/H_2O dyed with rhodamine B, silicone oil dyed with diesel colorant, and writing ink. (e) SEM view and EDX elemental distribution of GPS coated with LA. (f) Compressive stress−strain curves of GPS coated with different concentrations of PVA−TA/H_2O. (g) Calculated effective compressive modulus at strains of 0−60 and 60−80% corresponding to panel f. (h) Compressive test of GPS coated with PVA (30 wt %) from different directions. (i) Normalized value of GPS coated with LA for a piezoresistive and capacitive sensor. (j) Mechanical stiffness and electrical sensitivity reconfiguring of GPS via combining self-sucked coating with solvent erasing. The compressive strain was 30%.

allowing the generated gases (CO_2, H_2O, and NH_3) to merge and float.

When the NH_4HCO_3 concentration is varied, the effective compressive moduli of 60−80% strain are 1 or 2 orders of magnitude larger than that of 0−60% strain (panels d and e of Figure 3). The trend increases and then decreases with incremental NH_4HCO_3. Through Figure 3f and Figures S8 and S10 of the Supporting Information, large-sized pores and a more chaotic distribution are observed in GPS with 2.5 g of NH_4HCO_3 compared to those in other conditions. In such a case, less added NH_4HCO_3 (weaker inhibition of Pt) leads to faster solidification of PDMS and, hence, less time for floating and merging of bubbles. With more NH_4HCO_3 (over 5 g), the inhibition effect of −NH− aggravates, and it takes more time for the mixture to be cured, which results in generated bubbles escaping away and, hence, the pore gradient decreasing.

To further learn about gradient pores, a porous structure was cut into three parts for compression tests (Figure 3g). With applied pressure, the bottom part bears the highest stress

because of the small-sized pores, while the top part shows the lowest stress because of the large-sized pores. Moreover, with application from normal and tangential directions on a pristine GPS and a GPS without a stiff subsurface layer, compressive tests were conducted (Figure 3h). The orange curve shows the maximum stress, which is induced by the original stiff subsurface layer (with few pores). The blue and red curves show similar stress, while the green curve shows the minimum stress, which reflects a gradient pore distribution in the longitudinal direction yet a uniform distribution in the transverse direction. Additionally, curing time influences its mechanical stiffness as well (Figure 3i). With a longer heating time, GPS exhibits a stiffer compressive modulus.

Enabling Functionalities and Reconfiguration. With the air permeability checked for 7 days (Figure 4a and Figure S11 of the Supporting Information), various GPSs show a high permeability (>85%), indicating an inner-connected hollow structure. Such a structure contributes to continuous liquid infusion when the GPS is repetitively pressed and rebounded,
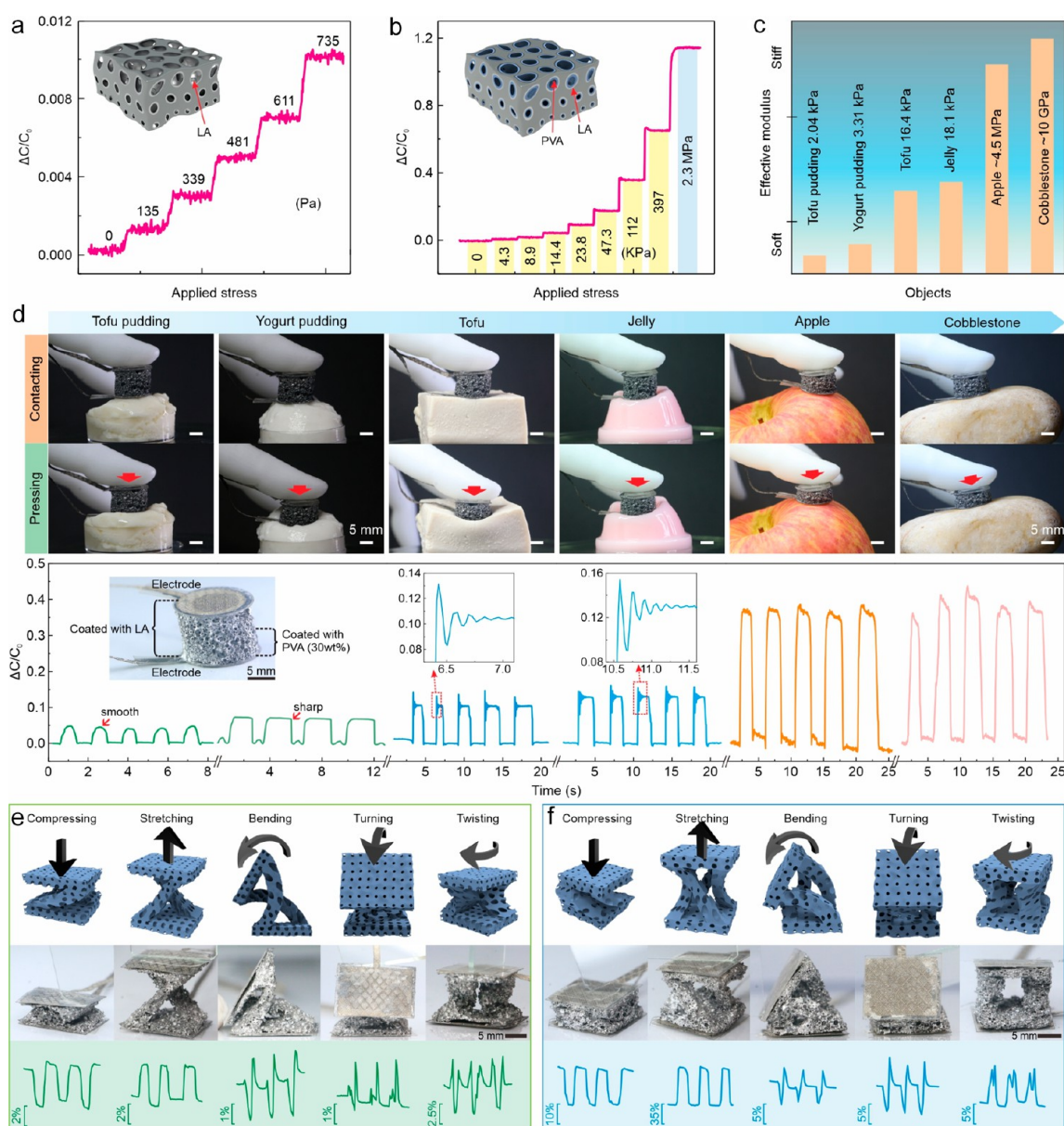
Figure 5. Object recognition and multimodal compliant mechanism with GPSs. (a) Tiny pressure detection via the GPS coated with LA. (b) Normalized capacitance under a broad range of pressures with the GPS coated with LA and PVA. (c) Effective moduli of various objects from ultrasoft to rigid (tofu pudding, yogurt pudding, tofu, jelly, apple, and cobblestone). (d) Different normalized capacitances by contacting and pressing various objects with hierarchically coated GPS (inset). (e and f) Schematic, various deformation modes, and corresponded normalized electrical resistance of the unstable compliant mechanism established by the GPS bulk with (e) two beams and (f) four beams.

hereafter, so-called self-sucked coating (Figure 4b). Four kinds of liquids with different viscosity and surface tension, e.g., LA, PVA−TA/H_2O, silicone oil, and writing ink, were employed for coating (Figure 4c). To visualize the coating process, dying was conducted on PVA−TA/H_2O and silicone oil with rhodamine B and diesel colorant, respectively. Through overall and cross-sectional images, we observe uniform and substantial colors on the inner surfaces of GPSs (Figure 4d and Figure S12 of the Supporting Information). Simultaneously, FSEM views and EDX elemental mapping of GPS coated with LA and PVA together with LA are shown in Figure 4e and Figure S13 of the Supporting Information, respectively. Abundant elements are observed and cover the surfaces of pores.

To further tune the stiffness of GPS (taking that with 0.5 g of LA−5 g of NH_4HCO_3 as an example), different

concentrations of PVA−TA/H_2O solution are employed (Figure 4f), and the corresponding effective moduli are shown in Figure 4g. With the coating of a higher concentration of PVA−TA/H_2O, GPS shows higher stiffness and effective modulus and, hence, brings a broad stiffness tunability ranging from ∼20 kPa to ∼2.7 MPa. However, when force is applied from different directions, an anisotropic compressing test shows a smaller difference (Figure 4h). It indicates a significant enhancement of anisotropic global mechanical stiffness via PVA coating. In addition, LA together with PVA are employed to endow electrical properties, e.g., piezoresistive and capacitive properties (panels a and b of Figure S14 of the Supporting Information), which achieve a robust signal output under various compressive frequencies and strains (panels c−e of Figure S14 and panels a and b of Figure S15 of the
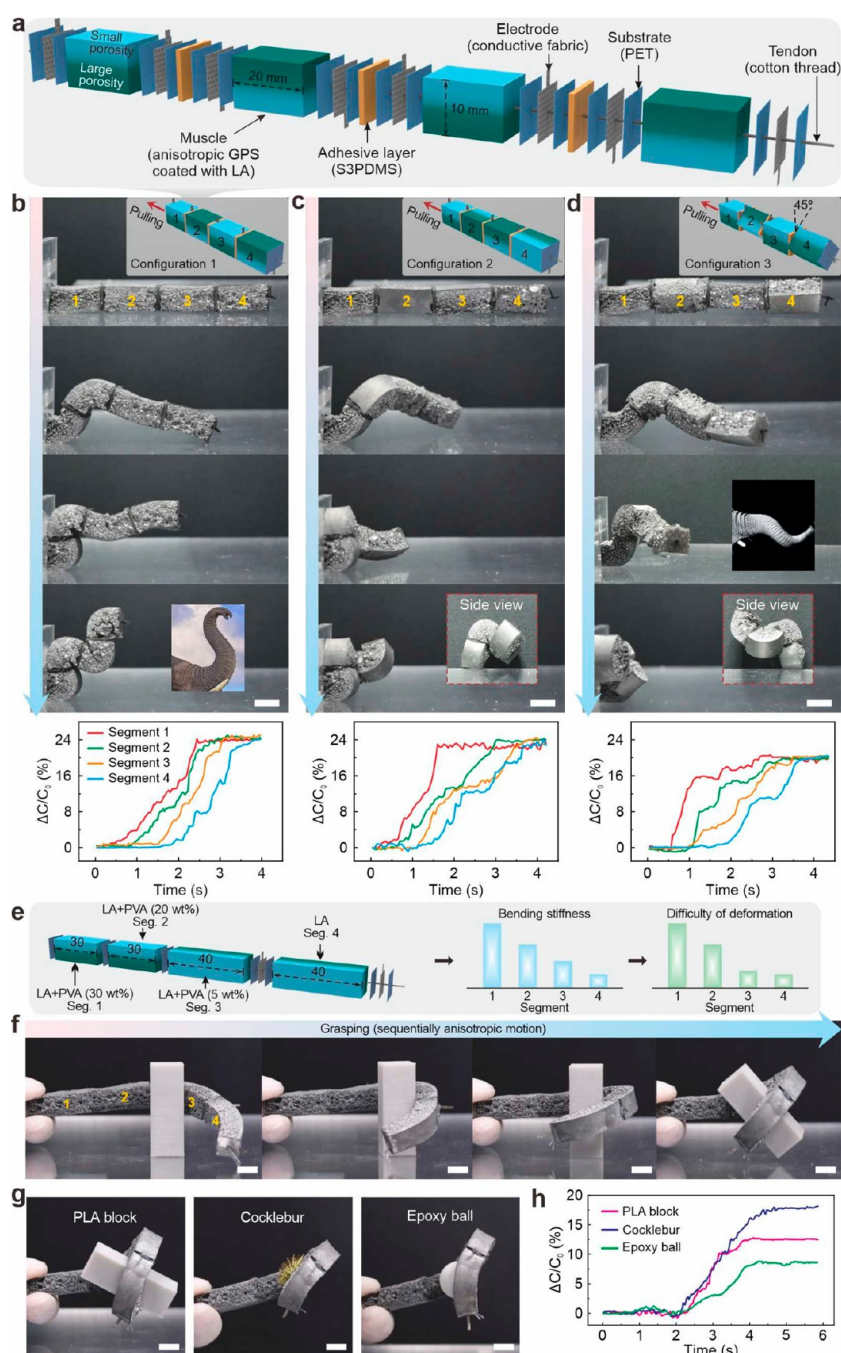
Figure 6. Tendon-driven biomimetic elephant trunk by assembly of anisotropic GPSs. (a) Explosive schematic. (b−d) Multimode of the reconfigurable GPS trunk, including configurations, images, and corresponding normalized capacitive change of each segment during deformations. (e) Schematically explosive illustration of the GPS trunk gripper and corresponding illustrated bending stiffness and degree of deformation of each segment. (f) Sequential images of the GPS trunk grasping a PLA block. (g) Images of the GPS trunk grasping a PLA block, a cocklebur, and an epoxy ball. (h) Normalized capacitive change of segment 4 during grasping. All scale bars are 10 mm.

Supporting Information). Thanks to gradient stiffness enhanced by PVA, the normalized resistance/capacitance shows anisotropic electrical sensitivity, of 0.013 and 0.04 kPa^{-1}, on normal and tangential directions (Figure 4i and Figure S15c of the Supporting Information). Furthermore, a 2000 cyclic test shows a consistent normalized capacity of GPS coated with LA and LA−PVA, which indicates high reliability of the GPS (Figure S15d of the Supporting Information).

In particular, the coated functional layer can be erased away by reimmersing in a proper solvent. Figure 4j demonstrates that the pristine GPS (state 1) is sequentially coated with LA

to obtain electrical response capability (state 2), and then erased in NaOH (aqueous, state 3). Subsequently, it is recoated with PVA/H$_2$O to obtain a higher stiffness (over 10 times, state 4) and finally erased in water (state 5). This process provides a reconfiguration of multifunctionalities of the porous bulk.

Demonstrations of Interactive Scenarios with Anisotropic Soft GPS Bulk. On the basis of integrated electrical sensing and tunable mechanical stiffness that are inherited from LA and PVA coating, GPS can be used for detecting various pressures/stresses, from 135 Pa to 2.3 MPa, which

indicates a wide range of force detection (panels a and b of Figure 5). Consequently, it provides a recognition of various objects with diverse stiffness, e.g., ultrasoft tofu pudding (effective modulus of 2.04 kPa) and super-rigid cobblestone (effective modulus of ~10 GPa) (Figure 5c). A hierarchically functionalized GPS globally coated with LA and partially coated with PVA (left inset in Figure 5d) was established to distinguish stiffness. From the inserted data in Figure 5d, when contacting and pressing tofu pudding with obvious fluidity, the detected capacitive curve is smooth, while when touching yogurt pudding with negligible fluidity, the curve is sharp. Such a distinct response hints at a feasible adaptability and dynamicity of the functionalized GPS detector and potential usage for distinguishing fluidic and colloidal objects. In comparison to the above two, tofu and jelly behave more elastic, which results in a non-negligible fluctuation when contacting them. It helps to distinguish elastic objects with a certain instability and resilience. The apple and cobblestone exhibit high stiffness, which induces great varied amplitude because the GPS is compressed up to the bottom stiff layer. These results suggest the possibility of objects being recognized by the on-demand coating of GPS. To exploit the feasibility of bulk construction of a soft robot, compliant mechanisms with a pair (Figure 5e) and two pairs (Figure 5f) of GPS beams were established. The PVA and LA integration endows the compliant structure with multimodal sensing, including compressing, stretching, bending, turning, and twisting, that matched with corresponding signal waveforms.

Furthermore, a tendon-driven biomimetic elephant trunk is demonstrated by assembling four anisotropic GPS muscles axially (Figure 6a). A S3PDMS[28] was employed to reversibly glue each muscle module during configuration switching. By reconfiguration of the combination of four GPS muscle segments, the biomimetic GPS trunk can achieve diverse anisotropic deformations (panels b−d of Figure 6 and Movie S2 of the Supporting Information). At the same time, the recorded capacitance real time reflects sequential changes from segments 1 to 4, because segment 1 was the closest to the fixed point on the condition of the same effective modulus of each segment. Therefore, to achieve on-demand sequential motion for object grasping, we tune the coating strategy and geometry of the GPS trunk accordingly (Figure 6e). From segments 1 to 4, a different concentrations of PVA endow each segment with different effective moduli and, thus, bending stiffness, which results in different degrees of deformation under the same force. Such an anisotropic configuration brings sequential motions from segments 4 to 1, which helps grasp various objects with diverse shapes and surface morphologies, such as a PLA block, a cocklebur, and an epoxy ball (panels f and g of Figure 6 and Movie S3 of the Supporting Information). During the grasping, the LA-coated segment 4 also timely reflects the capacitive signal change (Figure 6h). It suggests that our GPS offers a monolithic *in situ* proprioceptive sensing when constructing an anisotropically reconfigurable soft robotic bulk, with the combination of PVA and LA coating. This provides an elegant solution to construct a monolithically sensing-integrated structure with anisotropic feedback for future biomimetic soft robot fabrication.

In addition, such a collaborative action of PVA and LA with enhanced gradient stiffness and electrical sensing can help GPS to provide excellent mechanical buffering by its hierarchical strain response. During a free-falling test, varying from an ultralight cocklebur (0.18 g) to heavy LA (80 g), the GPS shows effective compression for absorbing the impact impulse with real-time signal output (Figure S16 of the Supporting Information). This test reveals a superior impulse absorption of GPS (up to 56.9 g m s^{-1}) when facing collision, providing an effective protection for soft robots when interacting with unexpected external objects.

CONCLUSION

The electron competitive−collaborative mechanism between elements of Ga (galinstan), N (NH_4HCO_3), and Pt (catalyst in the PDMS precursor) investigated here introduces a tunable gradient pore foaming strategy. The key findings are that (i) partial sedimented LA with a gradient distribution plays an important role in heterogeneous electron competition against NH_4HCO_3 and Pt, leading to gradient foaming; (ii) mechanical construction and morphology (slope of the pore gradient) of GPS could be preliminarily adjusted by varying the mixing ratio of the above three components; and (iii) interconnected open-pore network induced by widespread NH_4HCO_3 opens up a new opportunity for further endowing and reconfiguring functionality, including a tunable mechanical stiffness and integrated piezoresistive/capacitive layer, by means of self-sucked coating PVA and LA, respectively. Such a competition−collaboration mechanism not only offers an optional way for tuning similar polymerization processes with the hydrosilylation reaction, but the demonstrations of distinguishing objects, impact absorption, multimodal compliant structures, and proprioceptive sensing-integrated structure also validate the potential of GPS when acting as anisotropic interacting interfaces and bulk structures of soft robots enabled with tunable and reconfigurable stiffness monolithic-integrated diverse functionalities.

ASSOCIATED CONTENT

Ⓢ Supporting Information

The Supporting Information is available free of charge at https://pubs.acs.org/doi/10.1021/acsami.2c12384.

> Observation of the pore distribution (Figure S1), statistic size distribution (Figure S2), schematic of the multiphase mixture placing process (Figure S3), multi-dimensional μCT-reconfigured images (Figure S4), schematics of the hydrosilylation reaction in PDMS polymerization (Figure S5), weight change of $NaHCO_3$ and NH_4HCO_3 under 120 °C (Figure S6), statistic of control experiments (Figure S7), cross-sectional images of GPS with different combinations of LA and NH_4HCO_3 (Figure S8), radii and distribution of pores with varying LA contents (Figure S9), radii and distribution of pores with varying NH_4HCO_3 contents (Figure S10), air permeability test (Figure S11), self-sucked coating with various solutions (Figure S12), SEM images and EDX elemental distribution (Figure S13), electrical performance of GPS coated with LA and PVA (Figures S14 and S15), and compliant GPS for impact absorption (Figure S16) (PDF)

> Brief introduction of GPS: formation mechanism, properties, and demonstrations (Movie S1) (MP4)

> Anisotropically reconfigurable proprioceptive GPS trunk (Movie S2) (MP4)

> Biomimetic proprioceptive GPS trunk grasping various objects (Movie S3) (MP4)

■ AUTHOR INFORMATION

Corresponding Authors

Shuo Zhang − *State Key Laboratory of Digital Manufacturing Equipment and Technology, School of Mechanical Science and Engineering, Huazhong University of Science and Technology, Wuhan, Hubei 430074, People's Republic of China*; Email: shuo_zhang@hust.edu.cn

Zhigang Wu − *State Key Laboratory of Digital Manufacturing Equipment and Technology, School of Mechanical Science and Engineering, Huazhong University of Science and Technology, Wuhan, Hubei 430074, People's Republic of China*; orcid.org/0000-0002-3719-406X; Email: zgwu@hust.edu.cn

Authors

Zisheng Zong − *State Key Laboratory of Digital Manufacturing Equipment and Technology, School of Mechanical Science and Engineering, Huazhong University of Science and Technology, Wuhan, Hubei 430074, People's Republic of China*

Chuan Fei Guo − *Department of Materials Science and Engineering, Southern University of Science and Technology, Shenzhen, Guangdong 518000, People's Republic of China*

Han Ding − *State Key Laboratory of Digital Manufacturing Equipment and Technology, School of Mechanical Science and Engineering, Huazhong University of Science and Technology, Wuhan, Hubei 430074, People's Republic of China*

Complete contact information is available at:
https://pubs.acs.org/10.1021/acsami.2c12384

Author Contributions

[†]Shuo Zhang and Zisheng Zong contributed equally to this work.

Author Contributions

Shuo Zhang and Zhigang Wu conceived the idea. Shuo Zhang, Zisheng Zong, and Zhigang Wu designed the study. Shuo Zhang and Zisheng Zong designed and conducted the experiment and analyzed the data. Zhigang Wu, Han Ding, and Chuan Fei Guo supervised the study. Shuo Zhang, Zisheng Zong, and Zhigang Wu wrote the manuscript with input from all authors.

Notes

The authors declare no competing financial interest.

■ REFERENCES

(1) Rus, D.; Tolley, M. T. Design, Fabrication and Control of Soft Robots. *Nature* **2015**, *521* (7553), 467−475.

(2) Laschi, C.; Mazzolai, B.; Cianchetti, M. Soft Robotics: Technologies and Systems Pushing the Boundaries of Robot Abilities. *Sci. Robot.* **2016**, *1* (1), eaah3690.

(3) Miriyev, A.; Kovač, M. Skills for Physical Artificial Intelligence. *Nat. Mach. Intell.* **2020**, *2* (11), 658−660.

(4) Paul, C. Morphological Computation. *Robot. Auton. Syst.* **2006**, *54* (8), 619−630.

(5) Yang, G.-Z.; Bellingham, J.; Dupont, P. E.; Fischer, P.; Floridi, L.; Full, R.; Jacobstein, N.; Kumar, V.; McNutt, M.; Merrifield, R.; Nelson, B. J.; Scassellati, B.; Taddeo, M.; Taylor, R.; Veloso, M.; Wang, Z. L.; Wood, R. The Grand Challenges of *Science Robotics*. *Sci. Robot.* **2018**, *3* (14), eaar7650.

(6) Naleway, S. E.; Porter, M. M.; McKittrick, J.; Meyers, M. A. Structural Design Elements in Biological Materials: Application to Bioinspiration. *Adv. Mater.* **2015**, *27* (37), 5455−5476.

(7) Kim, S.; Laschi, C.; Trimmer, B. Soft Robotics: A Bioinspired Evolution in Robotics. *Trends Biotechnol.* **2013**, *31* (5), 287−294.

(8) Li, Y.; Fu, Z.-Y.; Su, B.-L. Hierarchically Structured Porous Materials for Energy Conversion and Storage. *Adv. Funct. Mater.* **2012**, *22* (22), 4634−4667.

(9) Gao, S.; Jia, X.; Yang, J.; Wei, X. Hierarchically Micro/ Nanostructured Porous Metallic Copper: Convenient Growth and Superhydrophilic and Catalytic Performance. *J. Mater. Chem.* **2012**, *22* (40), 21733−21739.

(10) Clarke, A.; Blake, T. D.; Carruthers, K.; Woodward, A. Spreading and Imbibition of Liquid Droplets on Porous Surfaces. *Langmuir* **2002**, *18* (8), 2980−2984.

(11) Zhuo, Y.; Wang, F.; Xiao, S.; He, J.; Zhang, Z. One-Step Fabrication of Bioinspired Lubricant-Regenerable Icephobic Slippery Liquid-Infused Porous Surfaces. *ACS Omega* **2018**, *3* (8), 10139−10144.

(12) Slater, A. G.; Cooper, A. I. Function-Led Design of New Porous Materials. *Science* **2015**, *348* (6238), aaa8075.

(13) Kang, S.; Lee, J.; Lee, S.; Kim, S.; Kim, J.-K.; Algadi, H.; Al-Sayari, S.; Kim, D.-E.; Kim, D.; Lee, T. Highly Sensitive Pressure Sensor Based on Bioinspired Porous Structure for Real-Time Tactile Sensing. *Adv. Electron. Mater.* **2016**, *2* (12), 1600356.

(14) Hartmann, M.; Schwieger, W. Hierarchically-Structured Porous Materials: From Basic Understanding to Applications. *Chem. Soc. Rev.* **2016**, *45* (12), 3311−3312.

(15) Wu, L.; Li, Y.; Fu, Z.; Su, B. L. Hierarchically Structured Porous Materials: Synthesis Strategies and Applications in Energy Storage. *Natl. Sci. Rev.* **2020**, *7* (11), 1667−1701.

(16) Sadasivuni, K. K.; Cabibihan, J.-J.; Deshmukh, K.; Goutham, S.; Abubasha, M. K.; Gogoi, J. P.; Klemenoks, I.; Sakale, G.; Sekhar, B. S.; Rama Sreekanth, P. S.; Rao, K. V.; Knite, M. A Review on Porous Polymer Composite Materials for Multifunctional Electronic Applications. *Polym.-Plast. Technol. Mater.* **2019**, *58* (12), 1253−1294.

(17) Wu, J.; Xu, F.; Li, S.; Ma, P.; Zhang, X.; Liu, Q.; Fu, R.; Wu, D. Porous Polymers as Multifunctional Material Platforms toward Task-Specific Applications. *Adv. Mater.* **2019**, *31* (4), 1802922.

(18) Yadav, R.; Baskaran, T.; Kaiprathu, A.; Ahmed, M.; Bhosale, S. V.; Joseph, S.; Al-Muhtaseb, A. H.; Singh, G.; Sakthivel, A.; Vinu, A. Recent Advances in the Preparation and Applications of Organo-Functionalized Porous Materials. *Chem. Asian J.* **2020**, *15* (17), 2588−2621.

(19) Thompson, B. R.; Horozov, T. S.; Stoyanov, S. D.; Paunov, V. N. Hierarchically Structured Composites and Porous Materials from Soft Templates: Fabrication and Applications. *J. Mater. Chem. A* **2019**, *7* (14), 8030−8049.

(20) Nam, Y. S.; Park, T. G. Porous Biodegradable Polymeric Scaffolds Prepared by Thermally Induced Phase Separation. *J. Biomed. Mater. Res.* **1999**, *47* (1), 8−17.

(21) Yang, X.-Y.; Chen, L.-H.; Li, Y.; Rooke, J. C.; Sanchez, C.; Su, B.-L. Hierarchically Porous Materials: Synthesis Strategies and Structure Design. *Chem. Soc. Rev.* **2017**, *46* (2), 481−558.

(22) Yang, J.; Tang, D.; Ao, J.; Ghosh, T.; Neumann, T. V.; Zhang, D.; Piskarev, Y.; Yu, T.; Truong, V. K.; Xie, K.; Lai, Y. C.; Li, Y.; Dickey, M. D. Ultrasoft Liquid Metal Elastomer Foams with Positive and Negative Piezopermittivity for Tactile Sensing. *Adv. Funct. Mater.* **2020**, *30* (36), 2002611.

(23) Mu, X.; Bertron, T.; Dunn, C.; Qiao, H.; Wu, J.; Zhao, Z.; Saldana, C.; Qi, H. J. Porous Polymeric Materials by 3D Printing of Photocurable Resin. *Mater. Horiz.* **2017**, *4* (3), 442−449.

(24) Jakus, A. E.; Geisendorfer, N. R.; Lewis, P. L.; Shah, R. N. 3D-printing Porosity: A New Approach to Creating Elevated Porosity Materials and Structures. *Acta Biomater.* **2018**, *72*, 94−109.

(25) Nam, Y. S.; Yoon, J. J.; Park, T. G. A Novel Fabrication Method of Macroporous Biodegradable Polymer Scaffolds Using Gas Foaming Salt as A Porogen Additive. *J. Biomed. Mater. Res.* **2000**, *53* (1), 1−7.

(26) Mac Murray, B. C.; An, X.; Robinson, S. S.; van Meerbeek, I. M.; O'Brien, K. W.; Zhao, H.; Shepherd, R. F. Poroelastic Foams for Simple Fabrication of Complex Soft Robots. *Adv. Mater.* **2015**, *27* (41), 6334−6340.

(27) Salerno, A.; Oliviero, M.; Di Maio, E.; Iannace, S.; Netti, P. A. Design of Porous Polymeric Scaffolds by Gas Foaming of Heterogeneous Blends. *J. Mater. Sci.: Mater. Med.* **2009**, *20* (10), 2043−2051.

(28) Jeong, S. H.; Zhang, S.; Hjort, K.; Hilborn, J.; Wu, Z. PDMS-Based Elastomer Tuned Soft, Stretchable, and Sticky for Epidermal Electronics. *Adv. Mater.* **2016**, *28* (28), 5830−5836.

(29) Zhang, S.; Wang, B.; Jiang, J.; Wu, K.; Guo, C. F.; Wu, Z. High-Fidelity Conformal Printing of 3D Liquid Alloy Circuits for Soft Electronics. *ACS Appl. Mater. Interfaces* **2019**, *11* (7), 7148−7156.

(30) Zheng, Y.; He, Z.; Gao, Y.; Liu, J. Direct Desktop Printed-Circuits-on-Paper Flexible Electronics. *Sci. Rep.* **2013**, *3* (1), 1786.

(31) Dickey, M. D.; Chiechi, R. C.; Larsen, R. J.; Weiss, E. A.; Weitz, D. A.; Whitesides, G. M. Eutectic Gallium-Indium (EGaIn): A Liquid Metal Alloy for the Formation of Stable Structures in Microchannels at Room Temperature. *Adv. Funct. Mater.* **2008**, *18* (7), 1097−1104.

(32) Carlborg, C. F.; Haraldsson, T.; Cornaglia, M.; Stemme, G.; van der Wijngaart, W. A High-Yield Process for 3-D Large-Scale Integrated Microfluidic Networks in PDMS. *J. Microelectromech. Syst.* **2010**, *19* (5), 1050−1057.

(33) Guibal, E. Interactions of Metal Ions with Chitosan-Based Sorbents: A Review. *Sep. Purif. Technol.* **2004**, *38* (1), 43−74.

(34) Dash, M.; Chiellini, F.; Ottenbrite, R. M.; Chiellini, E. Chitosan-A versatile Semi-Synthetic Polymer in Biomedical Applications. *Prog. Polym. Sci.* **2011**, *36* (8), 981−1014.

(35) Li, X.; Wang, Z.; Dong, G. Preparation of Nanoscale Liquid Metal Droplet Wrapped with Chitosan and Its Tribological Properties as Water-Based Lubricant Additive. *Tribol. Int.* **2020**, *148*, 106349.

📖 Recommended by ACS

Intrinsically Stretchable Microbattery with Ultrahigh Deformability for Self-Powering Wearable Electronics

Chong Bai, Desheng Kong, *et al.*

OCTOBER 26, 2022
ACS MATERIALS LETTERS   READ ☑

Flexible and Transparent Triboelectric Nanogenerators Based on Polyoxometalate-Modified Polydimethylsiloxane Composite Films for Harvesting Biomechanical Energy

Ying Su, Qingxin Tang, *et al.*

SEPTEMBER 28, 2022
ACS APPLIED NANO MATERIALS   READ ☑

PDMS Surface-Area Optimization for High-Performance Oscillatory Motion Harvesting Pendulum-Type Triboelectric Nanogenerators for Energy Harvesting and Sensor Applic...

Jong Beom Jang, Jae Su Yu, *et al.*

NOVEMBER 28, 2022
ACS APPLIED ELECTRONIC MATERIALS   READ ☑

Ferroelectricity-Coupled 2D-MXene-Based Hierarchically Designed High-Performance Stretchable Triboelectric Nanogenerator

Sujoy Kumar Ghosh, Hyunhyub Ko, *et al.*

JULY 14, 2022
ACS NANO   READ ☑

Get More Suggestions >